Self-healing SEI enables full-cell cycling of a silicon-majority anode with a coulombic efficiency exceeding 99.9%†

Yang Jin,‡[abc] Sa Li,‡[d] Akihiro Kushima,‡[b] Xiaoquan Zheng,[a] Yongming Sun,[c] Jin Xie,[c] Jie Sun,[c] Weijiang Xue,[b] Guangmin Zhou,[c] Jiang Wu,[a] Feifei Shi,[c] Rufan Zhang,[c] Zhi Zhu,[b] Kangpyo So,[b] Yi Cui*[ce] and Ju Li*[bd]

Despite active developments, full-cell cycling of Li-battery anodes with >50 wt% Si (a Si-majority anode, SiMA) is rare. The main challenge lies in the solid electrolyte interphase (SEI), which when formed naturally (nSEI), is fragile and cannot tolerate the large volume changes of Si during lithiation/delithiation. An artificial SEI (aSEI) with a specific set of mechanical characteristics is henceforth designed; we enclose Si within a TiO_2 shell thinner than 15 nm, which may or may not be completely hermetic at the beginning. *In situ* TEM experiments show that the TiO_2 shell exhibits 5× greater strength than an amorphous carbon shell. Void-padded compartmentalization of Si can survive the huge volume changes and electrolyte ingression, with a self-healing aSEI + nSEI. The half-cell capacity exceeds 990 mA h g^{-1} after 1500 cycles. To improve the volumetric capacity, we further compress SiMA 3-fold from its tap density (<0.4 g cm^{-3}) to 1.4 g cm^{-3}, and then run the full-cell battery tests against a 3 mA h cm^{-2} $LiCoO_2$ cathode. Despite some TiO_2 enclosures being inevitably broken, 2× the volumetric capacity (1100 mA h cm^{-3}) and 2× the gravimetric capacity (762 mA h g^{-1}) of commercial graphite anode is achieved in the stable full-cell battery cycling, with a stabilized areal capacity of 1.6 mA h cm^{-2} at the 100th cycle. The initial lithium loss, characterized by the coulombic inefficiency (CI), is carefully tallied on a logarithmic scale and compared with the actual full-cell capacity loss. It is shown that a strong, non-adherent aSEI, even if partially cracked, facilitates an adaptive self-repair mechanism that enables full-cell cycling of a SiMA, leading to a stabilized coulombic efficiency exceeding 99.9%.

Broader context

Nano silicon is the most promising alternative to the graphite anode for lithium-ion batteries due to its high theoretical capacity (4200 mA h g^{-1}). However, its fragile solid electrolyte interphase (SEI) cannot tolerate the large volume changes of bare Si, resulting in low coulombic efficiency. As shown in previous research studies, the yolk–shell design can effectively improve the coulombic efficiency. But like most nanoparticle-based powders, it faces the problem of low tap density. Even though the gravimetric capacity is impressive, the volumetric capacity would still be non-competitive compared to the commercial graphite anode. In this work, the speed and efficacy of self-repair of a crushed yolk–shell electrode have been systematically evaluated. It is shown that an exceptional degree of protection against liquid electrolyte flooding of nano Si can be eventually established, even though the number of cycles and the initial Li loss it takes to achieve this final condition are admittedly high. However, the final electrode thickness and volumetric/gravimetric specific capacities are still highly competitive against graphite. Highly compressed yolk–shell Si@TiO_2 nanotissue, despite unavoidable imperfections at the beginning, is resilient functionally and can achieve a high level of specific capacities and a stabilized coulombic efficiency at low cost, making lithium-constrained full-cell cycling of silicon-majority anodes (SiMAs) an imminent reality.

[a] *State Key Lab of Electrical Insulation and Power Equipment, School of Electrical Engineering, Xi'an Jiaotong University, Xi'an 710049, P. R. China*

[b] *Department of Nuclear Science and Engineering and Department of Materials Science and Engineering, Massachusetts Institute of Technology, Cambridge, MA 02139, USA. E-mail: liju@mit.edu*

[c] *Department of Materials Science and Engineering, Stanford University, Stanford, California, 94305, USA. E-mail: yicui@stanford.edu*

[d] *School of Materials Science and Engineering, Tongji University, 4800 Caoan Road, Shanghai 201804, China*

[e] *Stanford Institute for Materials and Energy Sciences, SLAC National Accelerator Laboratory, 2575 Sand Hill Road, Menlo Park, CA 94025, USA*

† Electronic supplementary information (ESI) available. See DOI: 10.1039/c6ee02685k

‡ These authors contributed equally to this work.

Introduction

Silicon is a promising alternative to the graphite anode for lithium-ion batteries because of its natural abundance, environmental friendliness, low discharge potential and high theoretical capacity (4200 A h kg^{-1} if $Li_{4.4}Si$).[1–3] However, the practical adoption of a Si-majority anode (SiMA), defined by Si occupying more than 50 wt% of the dried anode paste including binder and conductive agents, has been impeded by the enormous volume change (300–400%) and solid electrolyte interphase (SEI) instability experienced during lithiation/delithiation.[4–7] Because liquid electrolytes reductively decompose at the low working potential of Si (<0.5 V *versus* Li/Li^+), a passivating SEI layer always forms on any freshly exposed conductive surface. Such a SEI usually also contains non-cyclable (''dead'') lithium ions (LiF, Li_2O, *etc.*), trapped by irreversible side reactions.[8,9] Such a naturally formed SEI, which is fragile, easily breaks off and forms fluffy debris as the active content expands and contracts. This results in continuous consumption of the solvent molecules and cyclable (''live'') lithium,[10–13] so full-cell batteries with a SiMA or other high-capacity anodes (Al, Sn, *etc.*) often die quickly (within tens of cycles) because of Li- and/or solvent exhaustion. Therefore, ensuring SEI stability at the electrolyte–electrode interface is critical for long-life, lightweight Li-matched full cells. A variety of nanostructure designs have been developed to overcome the issues of mechanical breaking and spallation of the SEI.[14] Among them, the yolk–shell structure[15–22] has been shown to be an effective approach to stabilize fragile natural SEIs (nSEIs), by providing an artificial SEI (aSEI) layer support that does not expand/contract as much, even when the active materials encapsulated within do, as there is often void space left in between. This artificial SEI (for example thin-shell C and TiO_2) is often conductive to both electrons and Li ions, but stops the solvent molecules and large-sized anions like PF_6^- and $TSFI^-$.[23,24]

To survive the huge internal stress fluctuations and keep the liquid electrolyte away from the active material within the yolk–shell, three generic mechanical properties of the best aSEI encapsulation could be critical: (a) it should adhere weakly to stay semi-detached from the active material (*e.g.* Si), (b) is strong itself, and (c) adheres strongly to the nSEI that forms later. The aSEI should also be thin to be weight saving and have high ionic conductance. (a and b) are needed for load-isolation of a nSEI. If (a) is not true and the aSEI sticks too much with the Si, during ''steady-state'' cycling, too much of the dimensional change would be transferred to the aSEI and could cause it to break. (b) is also necessary because the aSEI layer would still sustain some load, especially at the contact points with Si which expands/shrinks, and it should not break at those points, just like good clothing should be made of strong fabric that does not stick to the body. Lastly, (c) is needed for self-healing, a central concept in the present paper. It turns out that, a nSEI, despite its fragility and softness and being the cause of low coulombic efficiency (CE) initially, is nonetheless self-healing and would work much better in combination with a strong aSEI.

Self-healing is a concept from biology, but may be generalized to some other dissipative emergent systems, where invasion can be adapted to *in situ* and the flaws get remedied sufficiently. Self-healing in the context of the yolk–shell SiMA means the following: if the aSEI enclosure is not completely hermetic and there are cracks in the shells (especially after being crushed to 1.4 g cm^{-3}, more than three times its tap density), inevitably liquid electrolyte would flow inside and inundate the Si. This seems catastrophic, as it could invalidate the whole yolk–shell design concept of isolating Si from the liquid electrolyte. But upon first lithiation with a reducing voltage, two things would happen: (i) there is solid nSEI formed on the TiO_2 shell and Si surface, and (ii) Si expands in volume due to lithiation, expelling liquid out of the cracks. Finally, the expanded Si + nSEI could touch the TiO_2 inner wall, and fresh nSEIs formed on both the surface of silicon and the TiO_2 shell, which will connect and ''caulk'' the crack, since a nSEI should adhere more strongly to TiO_2 than to Si under assumptions (a) and (c); see the illustrations in Fig. 1. Then upon first delithiation, the Si core would retract, leaving behind an *in situ* repaired artificial + natural SEI cocoon, sealing off and isolating the Si core from the liquid electrolyte. Self-healing in the present context thus means self-evacuating plus self-sealing.

The illustration in Fig. 1 is of course a gross simplification. In reality the repairs may be done in tens of cycles, and in some systems, full repair may never be done. In this paper we will track the coulombic efficiency (CE) as a quantitative indicator of the self-repair process. The CE, or rather the coulombic inefficiency (CI $\equiv 1 - CE$), is a measure of irreversible SEI growth per cycle. There is a battery industry lore that the stabilized CE needs to exceed 99.9% in order for a Li-matched (anode areal capacity $\approx$ cathode areal capacity) full-cell to cycle 200 times. However, many papers publish CE *vs.* cycle number n in a linear-scale plot, which hides valuable information about the self-healing process and nSEI accumulation. In this paper, we will carefully examine CI evolution on the logarithmic scale, to extract quantitative information about the major structural repairs that must happen in the first tens of cycles (the ''transient CE''), as well as the degree to which repair is eventually perfected to stop liquid electrolyte invasion (the ''stabilized CE'').

Amorphous carbon (aC) has been used as an aSEI in the yolk–shell design.[22–24] A TiO_2 nanoshell could be potentially superior to an aC shell in terms of (b) and (c).[25,26] With respect to (c), the polar nature of TiO_2 could mean stronger adhesion strength with the nSEI, which contains polar components LiF, Li_2O, *etc.* For (b), we will show experimentally that our TiO_2 nanoshell is much stiffer and stronger than an aC shell, and therefore is better for load-isolation. In our previous work,[27] it has been shown that TiO_2 is mechanically robust and an electrochemically high-performing aSEI, which supports full-cell cycling of Al nanoparticles encapsulated within, for hundreds of cycles, with greatly improved coulombic efficiency. The same will be demonstrated with Si cores here.

But like most nanoparticles-based materials, our Si@TiO_2 yolk–shell powder has a low tap density (<0.4 g cm^{-3}). Thus, even though the gravimetric capacity is very impressive

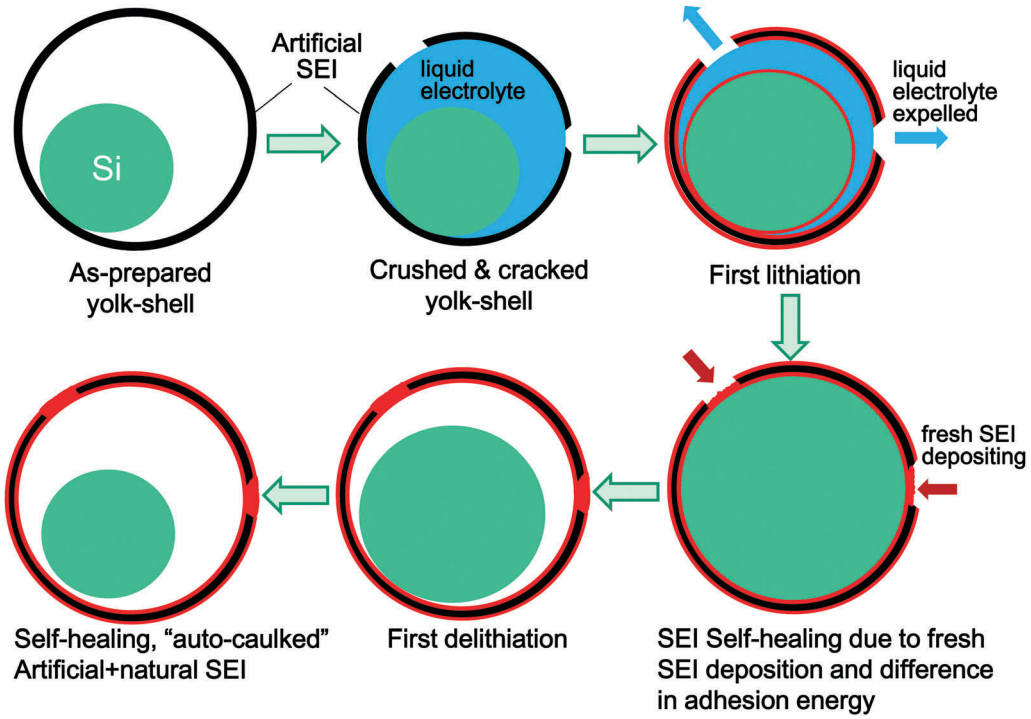

Fig. 1 Schematic illustrations of self-healing in a yolk–shell SiMA.

(~1000 mA h g^{-1} even after 1500 cycles in a half cell), the volumetric capacity would be much less impressive when compared with the commercial graphite anode, which has a compressed density of 1.4–1.8 g cm^{-3}. To further improve the SiMA's volumetric capacity for practical battery applications, we proceeded to compress the Si@TiO_2 yolk–shell powders to achieve an industrially relevant compressed density of 1.4 g cm^{-3}, which is more than three times its tap density (the pressing density was calculated based on the electrode as a whole, including binder, carbon black, and active materials). Some of the TiO_2 shells are inevitably cracked at such high applied pressures (>30 MPa). Surprisingly, this crushed SiMA material can still cycle stably in the full-cell configuration *vs.* commercial $LiCO_2$ cathode with an areal capacity rated at 3 mA h cm^{-2}, for one hundred cycles. In our full-cell tests, just a 14.7 μm-thick SiMA electrode provided an areal capacity of 1.6 mA h cm^{-2} (in contrast, a 55 μm thick commercial graphite electrode provided an areal capacity of 3 mA h cm^{-2}), which means we have achieved 2× the volumetric capacity of the commercial graphite anode at the slurry paste level (graphite: 550 mA h cm^{-3}, SiMA: 1100 mA h cm^{-3}), and more than 2× its gravimetric capacity (graphite: 340 mA h g^{-1}, SiMA: 762 mA h g^{-1}) in the stable full-cell battery cycling (1.6 mA h cm^{-2}) at the 100th cycle. The volumetric capacity of the fully lithiated Si@TiO_2 anode is still as high as 930 mA h cm^{-3}. This paper explains this experiment in detail and attempts to reveal the generic reasons behind the surprising phenomenon, that is, how can the yolk–shell nanostructure take the big crunch and still give an excellent coulombic efficiency and practical high performance in steady-state, full-cell cycling.

Results and discussion

Synthesis of a TiO_2 artificial SEI shell enclosing a Si yolk

The yolk–shell Si@TiO_2 cluster was synthesized *via* a two-step solution process. As schematically illustrated in Fig. 2a, low-cost glucose was used to coat Si. In previous reports without Si nanoparticles, aqueous glucose solution can produce monodisperse colloidal carbon spheres with functional groups such as –OH and –COOH on the surface under hydrothermal conditions.[29–32] In our case, once Si nanoparticles were added to the aqueous glucose solution, they acted as single-burst nucleation sites and organic carbon layers grew uniformly on the silicon surface. The final size of Si@C can be easily tuned by varying the hydrothermal time and concentration of glucose.[33–35] Next, Si@C@TiO_2 was prepared by aging the Si@C in titanium isopropoxide solution. Titanium ions would be adsorbed by the functional groups (–OH and –COOH) and subsequently a uniform TiO_2 precursor coating was formed on the organic carbon shell.[29]

After calcining Si@C@TiO_2 in air, the carbon layer was removed and the TiO_2 precursor shell turned into an anatase shell. Many anatase shells also merge with each other, thus forming connected yolk–shell Si@TiO_2 clusters, like biological tissue that contains many adjacent cells. To optimize the thermal treatment, TG-DTA analysis was carried out (Fig. S3, ESI†). The TiO_2 shell first undergoes dehydration with a weight loss of 6% at 100–250 °C. Then with continuous heating of the carbon in air, an obvious weight loss of 78% could be observed between 250 and 540 °C, with two exothermic peaks, which belong to phase transformations of amorphous TiO_2 to anatase (430 °C), and anatase to rutile (560 °C), respectively. Based on

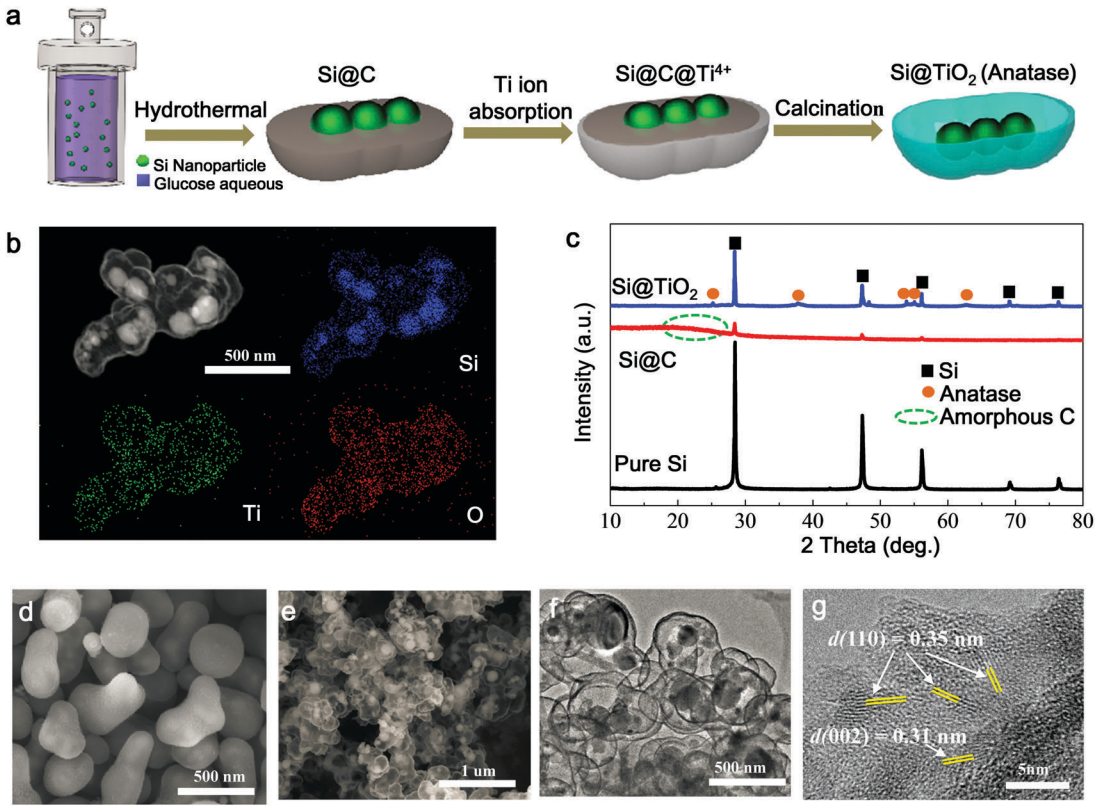

Fig. 2 Fabrication and characterization of the yolk–shell Si@TiO_2 cluster electrode. (a) Schematic of the synthesis of the yolk–shell Si@TiO_2 cluster. (b) STEM image and elemental mapping of Ti, O and Si, confirming the yolk–shell structure. (c) XRD data of the commercial nano silicon precursor, Si@C after hydrothermal treatment and the as-obtained Si@TiO_2 after 550 °C heat treatment in air. The organic layer was completely eliminated and the final product consists of pure silicon and anatase. (d) SEM image of Si@C@TiO_2 after titanium ion adsorption. (e and f) SEM and TEM images of the yolk–shell Si@TiO_2 cluster after heating at 550 °C in air for 2 h. TEM image shows that several Si nanoparticles are encapsulated in a continuous thin TiO_2 shell.

the TG-DTA results, the calcination conditions used in this study were 550 °C in air for 2.0 h, and the anatase TiO_2 shell is obtained. Fig. 2b shows a STEM image of the "Si@TiO_2 tissue", where silicon yolks were enclosed in the TiO_2 shell. The pristine commercial Si has a very thin oxidation layer (Fig. S4, ESI†). To verify whether nano Si will be oxidized severely during the 550 °C calcination, TG and XRD measurements of the pristine nano Si were collected. From Fig. S5 (ESI†) it can be seen that the increment of weight was less than 2.5% after 550 °C calcination in air, which will be much lower with the protection of the anatase shell. And no additional signal was found after calcination from the XRD results (Fig. S6, ESI†).

Elemental mapping verifies the presence of TiO_2 shells and Si yolks. XRD (Fig. 2c) demonstrates that the carbon is completely eliminated after thermal treatment in air and the final product consists of Si yolks and anatase nanoshells only. Fig. 2d–f show scanning electron microscopy (SEM) images and transmission electron microscopy (TEM) images of the Si@C@TiO_2 composite (Fig. 2d) and yolk–shell Si@TiO_2 (Fig. 2e and f). As revealed by high resolution TEM (Fig. 2g), the shell is continuous and the anatase lattice planes {110} and {002} can be identified. The weight ratio of Si and TiO_2 was calculated to be 73 : 27 (Si : TiO_2) based on the full Si oxidation experiment at 1200 °C (Fig. S7, ESI†).

Mechanical strength of the TiO_2 artificial SEI

To characterize the strength of the TiO_2 shell synthesized above, *in situ* TEM indentation experiments were performed on the aC and TiO_2 shells, as shown in Fig. 3a. An atomic force microscopy (AFM) cantilever probe (Nanosensors PPP-NCHR) (Fig. 3b) with a spring constant of 30 N m^{-1} was attached to the tip of the gold wire using a conducting epoxy (Chemtronics CW2400). aC and TiO_2 shells were attached to the tungsten probe with a conducting epoxy glue. The gold wire and the tungsten probe were then mounted on a Nanofactory™ STM-TEM holder. Using the 3D piezo-manipulator, the shell was brought into contact with the cantilever tip and compression was applied to the shell by imposing a displacement (D) against the cantilever. The force acting on the shell was calculated by measuring the cantilever deflection. For comparison, hollow TiO_2 and aC shells with nearly the same thickness and diameter were chosen for the AFM indentation experiment. Fig. 3c and d show the dynamic deformation of hollow aC and TiO_2 shells under compression until the shells crack. The force–displacement curve measured by the *in situ* TEM indenter is shown in Fig. 3e, and the stiffness of the TiO_2 and aC shell was calculated to be 500 N m^{-1} and 90 N m^{-1}, respectively.

The calendering process in commercial electrode fabrication is a big challenge for hollow nanostructured materials (yolk–shells,

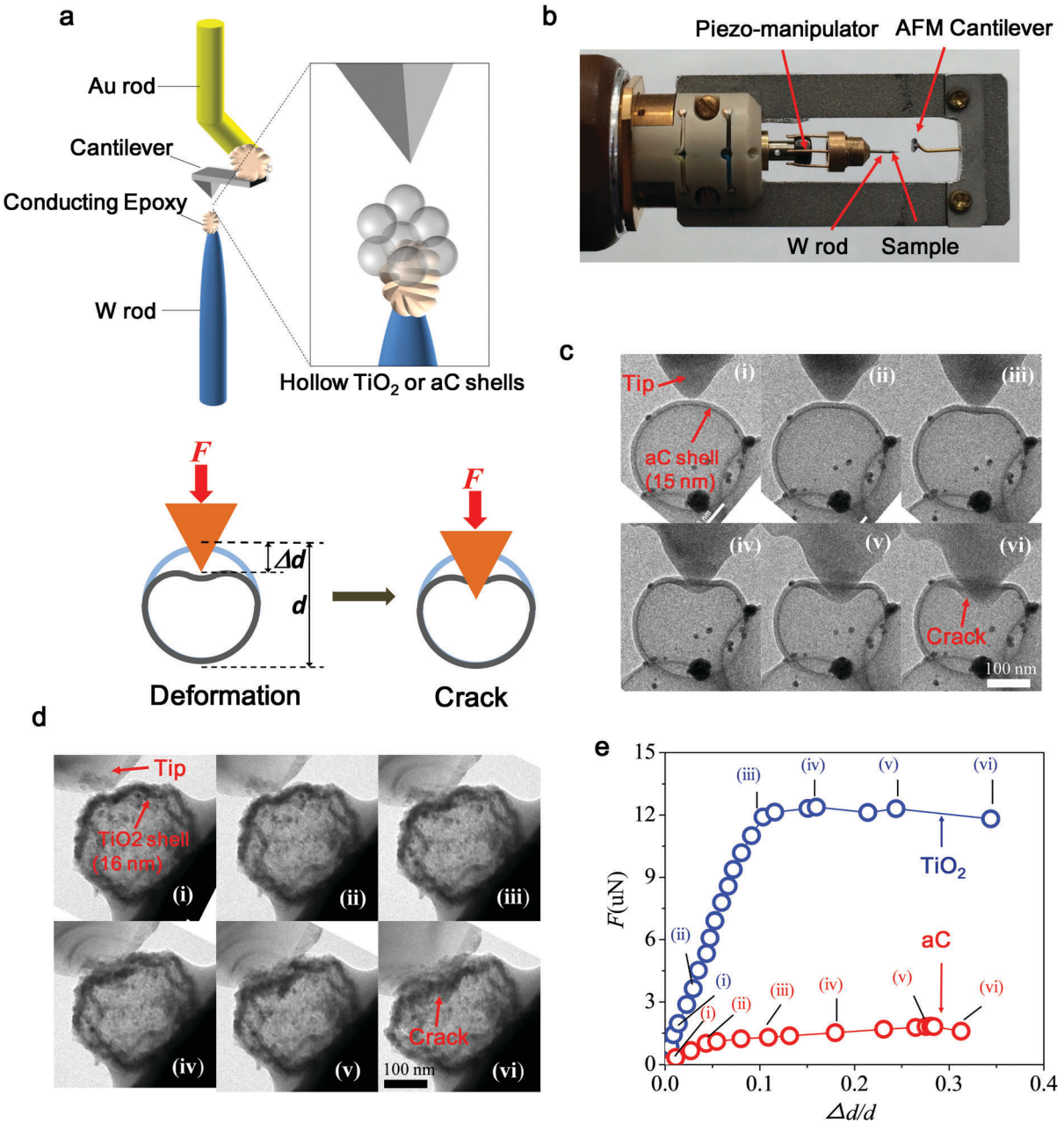

Fig. 3 *In situ* TEM indentation of a hollow TiO_2 shell and hollow aC shell. (a) Schematic. (b) Optical image of the *in situ* TEM indenter. (c and d) Dynamic deformation of the hollow TiO_2 shell and hollow aC shell under an applied force (Movie S1 and S2, ESI†). The diameter of the hollow TiO_2 shell is 230 nm and the thickness is 16 nm. The diameter of the hollow aC shell is 258 nm and the thickness is 15 nm. (e) Force *vs.* compression rate ($\Delta d/d$) of the hollow TiO_2 shell and hollow aC shell.

multi-shells, *etc.*), as the thin shells would sustain significant pressure (Fig. 4a). To examine the deformation and fracture of the yolk–shell "Si@TiO_2 tissue", a quantitative macroscopic pressing experiment was conducted. Fig. 4b is the SEM image of the Si@TiO_2 electrode. It is obvious that under the same macroscopic pressure, the Si@TiO_2 cluster maintains its structural integrity better than Si@aC (Fig. 4c), with which many more shells are completely destroyed. *In situ* TEM indentation of a μm-piece of "Si@TiO_2 tissue" also validates its superior mechanical robustness (see Movie S3, ESI†). After 41 MPa pressing, the Si@TiO_2 tissue did not break as a whole (Fig. 4d), and this overall structural robustness persists to a final pressure as high as 160 MPa (Fig. S8 and Movie S4, ESI†). Nonetheless, it is hard to ascertain (and indeed to believe) that the TiO_2 shells are all completely hermetic, as small cracks would be hard to detect by TEM.

Pressing low-density powders into higher-density electrodes

It is clear from Fig. 2e, f and 4b that the yolk–shell Si@TiO_2 cluster has a large interstitial volume. Even though some interstitial porosity is needed for the liquid electrolyte to

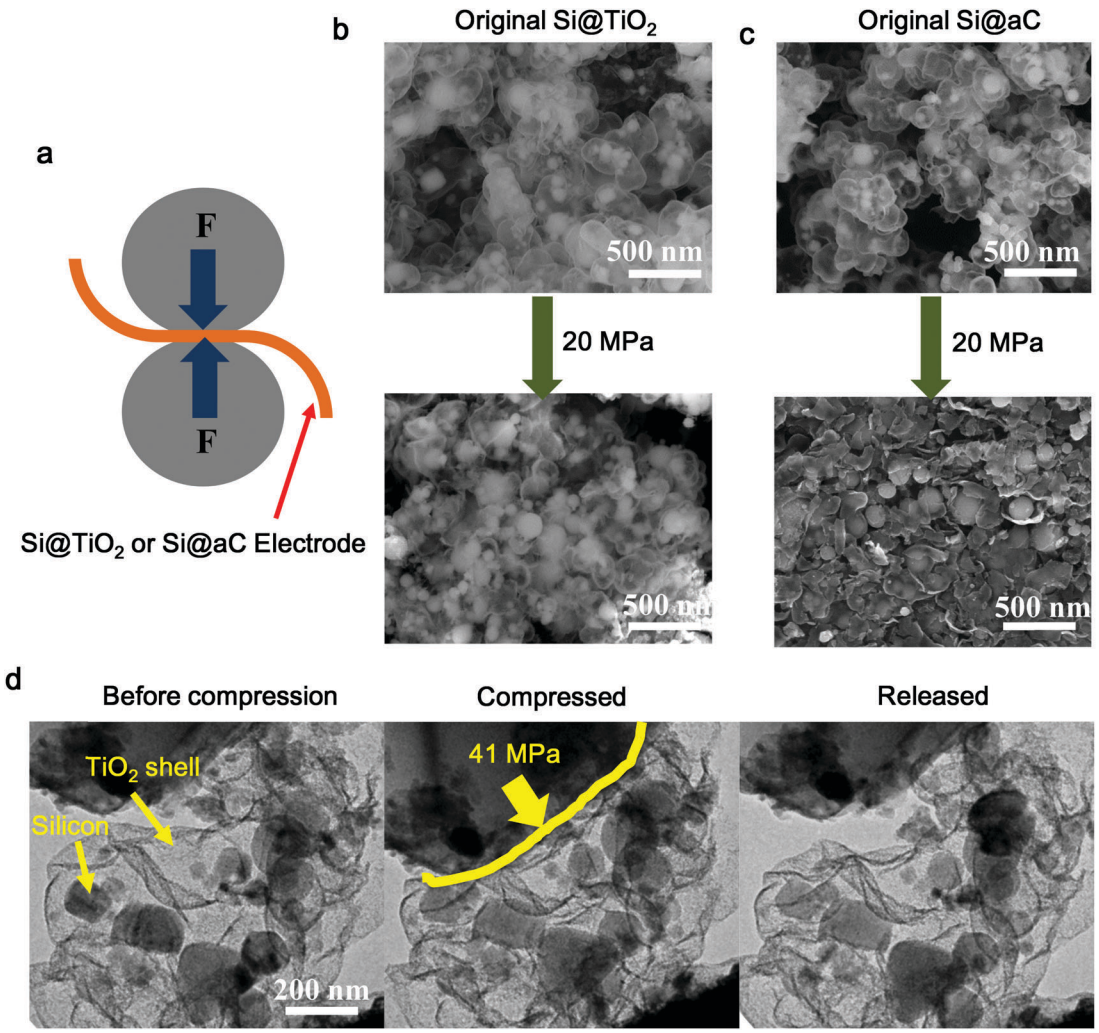

Fig. 4 Electrode and Si@TiO_2 nanocluster pressing experiment. (a) Schematic of the macroscopic electrode pressing. (b and c) SEM image of the Si@TiO_2 cluster and Si@aC electrode, original and after 20 MPa pressing. (d) *In situ* TEM press experiment of the yolk–shell Si@TiO_2 nanocluster. Left, middle, and right images correspond to the initial, compressed, and load released states, respectively. To obtain the stress, the load was calculated by the displacement of the AFM cantilever tip and the contact area was estimated to be a circular shape. See Movie S3 (ESI†).

percolate in the anode and enable long-range Li^+ conduction, the as-calcined powders have too low a density (<0.4 g cm^{-3}). In such an uncompressed state, even if the gravimetric specific capacity of Si@TiO_2 is exceedingly high and stable ($\sim$1000 mA h g^{-1}), it would still have a hard time competing with commercial low-cost graphite in terms of specific volumetric capacity, since the compressed density of the graphite anode (1.4–1.8 g cm^{-3}) would be 4× that of the as-made Si@TiO_2 powder. In order to compete with graphite, one must compress Si@TiO_2. Inevitably, a lot of TiO_2 shells will crack in the slurry making, pressing and calendaring. One could also argue that for the carbon precursor to leave the Si@TiO_2 clusters completely by oxidation (Fig. 2b and c), the TiO_2 shell cannot be completely hermetic at the beginning either. It is in view of such aSEI enclosures with defects, incurred by the necessities of sample and electrode preparations, that we evaluate the battery performance and coulombic inefficiency using hard-pressed electrodes.

SiMA half- and full-cell performance, and coulombic inefficiency as a diagnostic of the rapidity and thoroughness of seal-healing

The coulombic efficiency (CE) of an anode is defined as the ratio of the total oxidative charge (Q_{ox}) to reductive charge (Q_{re}) as it cycles up and down a fixed voltage range, say between U_{min} = 0.01 and U_{max} = 1.0 V.

$$CE_n \equiv \frac{Q_{ox}(n; U_{min}, U_{max})}{Q_{re}(n; U_{min}, U_{max})} \quad (1)$$

where n = 1, 2, 3,... is the cycle number. For a SiMA with no Li at the beginning, the sequence we measure from galvanostatic cycling is $Q_{re}(1)$, $Q_{ox}(1)$, $Q_{re}(2)$, $Q_{ox}(2)$, $Q_{re}(3)$, $Q_{ox}(3)$,..., and CE_1 is the initial cycle efficiency. If both the working and counter electrodes accept/eject only Li^+, then because of the requirement to maintain charge neutrality in the electrolyte, working, and counter electrode, respectively, $(1 - CE)Q_{re}$ Li^+ must arrive

at the tested electrode *via* the electrolyte from the counter electrode and not return, to compensate for the "lost electrons" metered on the outer circuit. So the coulombic inefficiency (CI),

$$\mathrm{CI}_n \equiv 1 - \mathrm{CE}_n \tag{2}$$

is an indicator of Li-transfer from the counter-electrode ("corroded") to the tested electrode ("plated") as a battery cycles up and down a fixed voltage range. For this potential range then, the transferred $\mathrm{CI}_n Q_{\mathrm{re}}(n)$ Li^+ in this cycle is likely physically converted from "live Li-ion" to "dead Li-ion" (at least "dead" for this fixed voltage range) embedded in the SEI, and following this assumption the total amount of "live Li-ion" in the cell will sustain an exponential decay with the number of cycles. This is the rationale for the battery industry lore of "the CE needs to be better than 99.9%", since $0.999^{200} \approx 0.8$, and 20% capacity fading is set as an industrial criterion for cell life. In reality, it could be even worse than this projection if Li cations are incorporated together with the salt anions into the SEI (for example, for each "lost electron", one free Li^+ cation and three $\mathrm{LiPF_6}$ are incorporated into the SEI of the tested anode), or under certain circumstances, it could be better than this projection if the electrolyte supports reversible shuttling.[27,28] With the caveats stated above, CI is commonly understood as a rough indicator of SEI growth and accumulation on the tested anode. CI_n usually decays with n. People often distinguish between "transient" coulombic efficiency, when the CI_n curve varies rapidly with n in the initial cycles, *vs.* "stabilized" coulombic efficiency:

$$\begin{aligned} \mathrm{CE}_{\mathrm{stablized}} &\equiv \lim_{n\to\infty} \frac{1}{2M+1} \sum_{n'=n-M}^{n+M} \mathrm{CE}_{n'}, \\ \mathrm{CI}_{\mathrm{stablized}} &\equiv \lim_{n\to\infty} \frac{1}{2M+1} \sum_{n'=n-M}^{n+M} \mathrm{CI}_{n'} \end{aligned} \tag{3}$$

where $2M + 1$ is a running-window average. In the context of self-sealing and self-healing, the "transient" CI_n curve represents how quickly the anode responds to initial electrolyte invasion and accomplishes major repairs of the structure to reduce flooding of the active content, in the first few tens of cycles. In contrast, $\mathrm{CI}_{\mathrm{stablized}}$ characterizes the degree of eventual repairedness and hermiticity of the protective structure as it constantly fights against the fluctuating stress and damage. In the battery industry, it is often demanded that the "transient" CI_n drops below 5×10^{-3} (CE > 99.5%) in less than 10 cycles (graphite accomplishes this in 5 cycles or less), reflecting the extreme rapidity of the self-healing of micron-scale commercial graphite particles. Another requirement is that $\mathrm{CI}_{\mathrm{stablized}}$ needs to be smaller than 1×10^{-3} ($\mathrm{CE}_{\mathrm{stablized}} >$ 99.9%) for the electrode to be considered commercially viable. From a full-cell performance perspective, $\mathrm{CE}_{\mathrm{stablized}} = 0.99$ ($\mathrm{CI}_{\mathrm{stablized}} = 0.01$) is indeed poor and signifies significant mechanical instabilities of the SEI (if reversible shuttling could be excluded), therefore plotting CE_n on a linear-scale hides really valuable diagnostic information. We recommend plotting CI_n on the log-scale (Fig. 6b, red symbols). In actual experiments, one can also measure negative CI_n data ($\mathrm{CE}_n > 1$), for example when CI gets very small and the noise rises up to instrumentation precision. For these n, we will just plot $-\mathrm{CI}_n$ on the log-scale, but with a different color (Fig. 6b, green symbols).

We would also like to define a "coulombic inefficiency cumulant (CIC)", as

$$\begin{aligned} \mathrm{CIC}_n &\equiv \frac{1}{Q_{\mathrm{re}}(1)}[Q_{\mathrm{re}}(1) - Q_{\mathrm{ox}}(1) \\ &\quad + Q_{\mathrm{re}}(2) - Q_{\mathrm{ox}}(2) + \cdots + Q_{\mathrm{re}}(n) - Q_{\mathrm{ox}}(n)] \\ &= \mathrm{CI}_1 + \frac{Q_{\mathrm{re}}(2)}{Q_{\mathrm{re}}(1)}\mathrm{CI}_2 + \cdots + \frac{Q_{\mathrm{re}}(n)}{Q_{\mathrm{re}}(1)}\mathrm{CI}_n \end{aligned} \tag{4}$$

which is the cumulant of "capacity-weighted" individual-cycle coulombic inefficiencies. If the coulombic inefficiency indeed reflects the "live Li" → "dead Li" conversion per cycle, CIC_n should numerically represent the total percentage of conversion from "live Li" → "dead Li" in a lithium-matched (initial anode areal capacity = initial cathode areal capacity) full-cell, *e.g.* the "live" lithium exhaustion fraction. In lithium-constrained full cells, how CIC_n increases with n should thus give us a good indication of how the full cell battery capacity decays with n, if lithium exhaustion is the main driver of (full-cell) capacity fade. We will test this hypothesis experimentally. To facilitate the comparison, let us also define the actually measured "capacity fade fraction"

$$F_n \equiv \frac{1}{Q_{\mathrm{re}}(1)}[Q_{\mathrm{re}}(1) - Q_{\mathrm{ox}}(n)] \tag{5}$$

which compares the nth-cycle discharge capacity with the first-cycle charge capacity, which is a practical metric. By contrasting (4) with (5), we note that if

$$Q_{\mathrm{re}}(n' + 1) = Q_{\mathrm{ox}}(n') \tag{6}$$

for all $n' < n$, then such a numerical comparison would be unnecessary because then mathematically

$$\mathrm{CIC}_n = F_n \tag{7}$$

We will show subsequently, with hard-pressed and partially cracked $\mathrm{Si@TiO_2}$ in a slurry-pasted electrode, that our full-cell battery gives $\mathrm{CIC}_n \approx F_n$, but not exactly, which means (6) does not hold up exactly in reality. Nonetheless, CIC_n and F_n are both computed based on experimental data and plotted against n and discussed, and their still significant agreement means the full-cell capacity fade is indeed mainly driven by "live Li" → "dead Li" conversions related to SEI growth.

For our materials, galvanostatic cycling from 0.01 to 1 V was performed in type 2032 coin cells. The $\mathrm{Si@TiO_2}$ electrode exhibits a remarkable performance in half cells against super-abundant lithium metal. As shown in Fig. 5a, at a rate of 0.05C, the first discharge and charge capacities are 2374 and 1562 mA h g^{-1}, respectively, giving an initial cycle $\mathrm{CE}_1 = 65.8\%$, and then the specific capacity stabilizes at 1070 mA h g^{-1} for later cycles at 0.5C. Even after 1500 cycles, the gravimetric capacity is 990 mA h g^{-1}. CE can reach 99% in the 6th cycle, and 99.5% in the 20th cycle. The voltage profiles for the

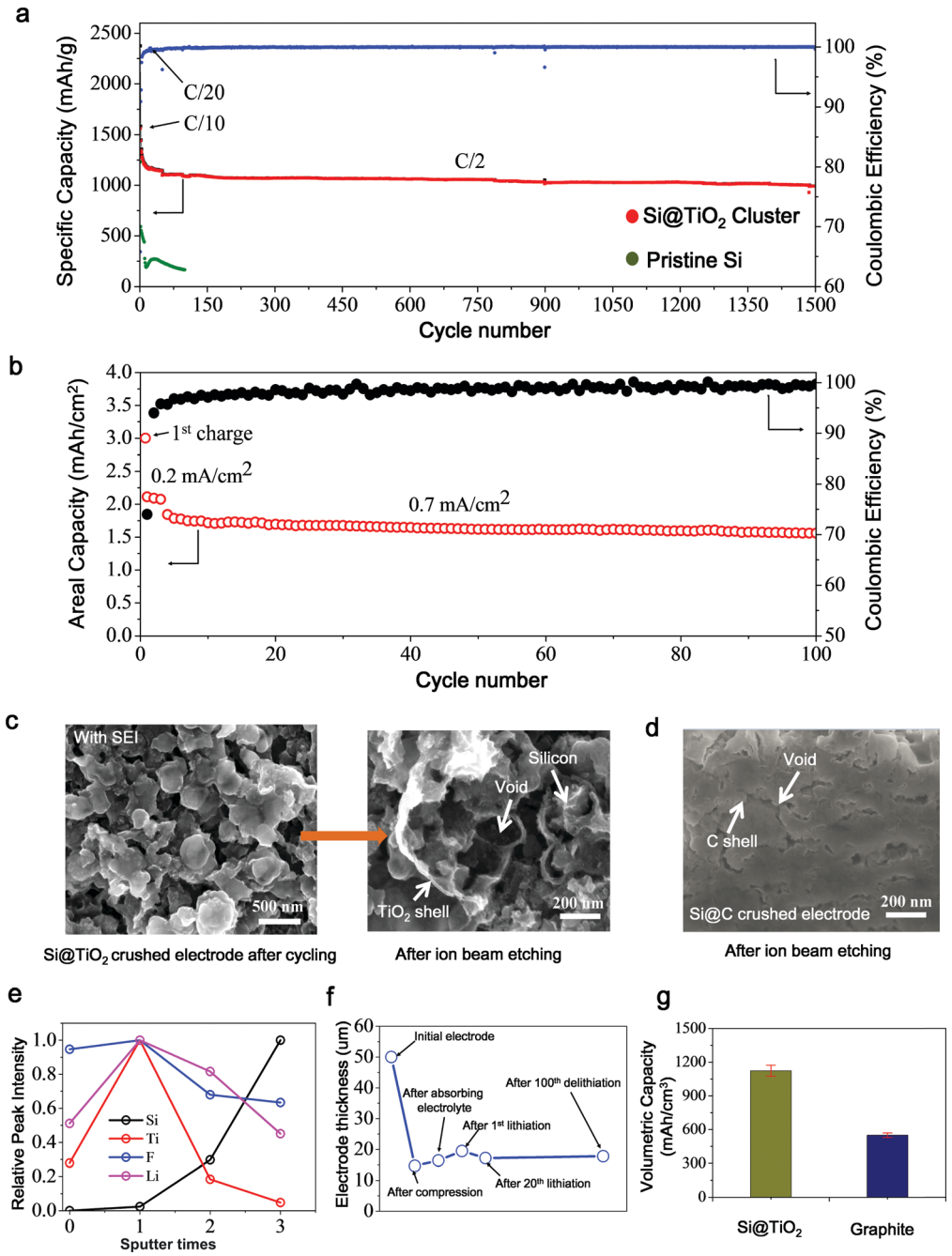

Fig. 5 Electrochemical characterization of the Si@TiO_2 pressed electrode. All specific capacities reported are based on the total mass of Si + TiO_2. (a) Cycling life and the corresponding coulombic efficiency over 1500 cycles. The charge/discharge rate was C/20 for the first cycle, then C/10 for the next 5 cycles, and C/2 (1C ≡ 4.2 A g^{-1} Si) for the following cycles. The mass loading of all active materials was about 0.8 mg cm^{-2}. (b) Full cell performance of the Si@TiO_2 cluster anode (2.1 mg cm^{-2}) paired with a lithium cobalt oxide cathode. (c) SEM image of the Si@TiO_2 crushed electrode (30 MPa) after 100 cycles (full cell); left part is with SEI and right part is after ion beam etching. (d) SEM image of the Si@aC crushed electrode (30 MPa) after 50 cycles. (e) Relative peak intensity (Si, Ti, F, and Li) of the Si@TiO_2 cluster electrode after 1500 cycles or discharging and charging, measured by X-ray photoelectron spectroscopy (XPS) for 3 ion sputtering times; time 0 means before sputtering. (f) Electrode thickness variation. (g) Volumetric specific capacity of Si@TiO_2 *vs.* commercial graphite.

different cycles are shown in Fig. S6 (ESI†). The shape of the profile does not change much from the 250th to the 1500th cycle, indicating the stable electrochemical behavior of the Si@TiO_2 cluster.

This cycling stability is attributed to the mechanically robust TiO_2 nanoshells. To further explore the structural integrity after 1500 cycles, we used X-ray photoelectron spectroscopy (XPS) to measure the spatial distribution of the elements (Si, Ti, F, Li) under ion sputtering. Each sputtering will strip away a certain thickness. As demonstrated in Fig. 5e, before sputtering, no Si signal could be detected while the intensity of Ti, F, Li (aSEI + nSEI elements) could be clearly seen. It is obvious that silicon

was still under the protection of the aSEI + nSEI. With increasing sputtering times, peak density of Si gradually becomes intense while Ti tails away, as the sputtering strips the aSEI + nSEI shells and exposes the inner silicon.

While the yolk–shell design can effectively extend the cycle life of silicon anodes and improve $CE_{stabilized}$, it suffers from a low transient CE_n (due to the larger surface area, the amount of SEI formed is large), and low tap density. Pre-lithiation is an effective approach to improve the low initial CE, even though the cost of pre-lithiation technology used by industry is still high. However, new and cheap pre-lithiation methods are being developed at laboratory scales.[36–38] Besides, electrolyte additives such as FEC and VC[39–41] can also improve the CE of the Si anode. On the other hand, the anode density could be improved by mechanical compression, which inevitably would crack some aSEIs, leading to non-hermiticity and electrolyte ingression. It is here that we expect the self-sealing and self-healing mechanism shown in Fig. 1 to play a central role.

To characterize the self-sealing ability of the Si@TiO_2 cluster electrode, a full-cell test, where the areal capacities of the anode and cathode are initially matched ("Li-matched") to be 3 mA h cm^{-2}, was conducted. A high pressure (30 MPa) was applied to press and make the Si@TiO_2 electrode. Fig. 5f shows the electrode thickness variation at different stages of preparation and usage. Before pressing, the thickness of Si@TiO_2 cast onto the Cu foil was 50 μm, which changed to 14.7 μm after pressing. After overnight immersion in EC/DEC electrolyte, the electrode thickness increases to 16 μm. Some TiO_2 encapsulations are inevitably cracked at such a high pressure (Fig. S9, ESI†). Surprisingly, the electrode shows excellent full cell performance. As shown in Fig. 5b, when paired with a commercial lithium cobalt oxide (LCO) cathode rated at 3 mA h cm^{-2}, the crushed Si@TiO_2 electrode exhibits stable cycling at industrially relevant levels of areal current density. At a high mass loading of the Si@TiO_2 cluster (2.1 mg cm^{-2}), with a first discharge capacity of $Q_{re}(1)$ = 3 mA h cm^{-2} to perfectly match that of commercial LCO cathode, a high areal capacity was attained (Fig. 5b, red circles), which is above 1.6 mA h cm^{-2} even after 100 cycles at 0.7 mA cm^{-2} (see voltage profile in Fig. S12, ESI†). In addition, the electrode thickness increased by 22% (16 → 19.5 μm) after the first lithiation. After the 20th cycle (lithiation stage), when the CE gets as high as 99.5%, the electrode thickness was about 17.2 μm (Fig. 5f). When the electrode was assembled in a coin cell, a spring was inserted to accommodate the pressure and electrode thickness variation. Such an external spring is a common feature used in solid electrolyte/Li metal batteries to maintain good contact: since our Si has a high capacity and volume change like Li metal, and because our aSEI + nSEI are solid electrolytes, we are well justified to use such spring loads as well (the spring stiffness is $\sim 10^4$ N m^{-1}). During the first delithiation process, because of the compressing force from the spring, the electrode shrinks and the thickness decreases. During the second lithiation process, some of the Si loses electrical contact and becomes inactive. These Si will not participate in the following lithiation/delithiation process, and fails to contribute to the volume expansion continuously, which is consistent with a capacity of 2.1 mA h cm^{-2}. The whole aSEI + nSEI framework needs some cycles to fully accommodate the Si volume change under the spring load, in a "shake-down" process. That is why the electrode thickness was increased during the first lithiation process and then decreased during the following cycles. Once the self-healing is done with a rigid hermetic solid-electrolyte skeleton around Si, the spring can be taken away. Fig. 5c shows the structure of the Si@TiO_2 cluster electrode after full cell cycling. The shell's outer surface becomes thicker and rougher after the battery cycling, indicating the coating of a nSEI on the TiO_2 shell. It is very important to explore the inner integrity of the nanostructured electrode. If the broken TiO_2 shell fails to self-seal, a nSEI will grow on the surface of silicon and continuously consume lithium. Accumulated nSEIs will occupy the inner empty space. Here, a focused ion beam (FIB) was used to cut the compressed Si@TiO_2 electrode (Fig. 5c right). After ion beam etching, it is clear that the inner void space still remains, like the survival space in post-earthquake crumbled buildings. The SEI must not grow on the inner silicon surface after self-healing of cracked TiO_2 shells, otherwise the accumulated SEI will occupy almost all of the inner space, as Fig. 5d shows for the crushed Si@aC electrode (30 MPa) after cycling, where nSEI debris completely fills up electrode. In contrast, a full-cell of Si@aC completely dies after tens of cycles. As the anatase shell was in the lithiated state during cycling, to further verify the mechanical strength of lithiated anatase structure, acid (0.5 M HCl) was used to remove the surface SEI. Even after 100 cycles, the yolk–shell structure was still maintained, indicating that the lithiated anatase shell was mechanically stable during the charge/discharge processes (Fig. S13, ESI†). Fig. S14a (ESI†) shows the electrode thickness after 100 cycles for the SiMA. From the 20th (lithiation stage) to 100th cycle (delithiation stage), the thickness increases by about 0.6 μm (3.4%), which means almost no electrode volume change during the later cycles, and a stable and hermetic aSEI + nSEI combination (Fig. 5f). For comparison, after 100 cycles, the electrode thickness increment of Si@aC is 66%, much higher than that of Si@TiO_2 (25.5%), which can be seen in Fig. S14b (ESI†). Based on the areal capacity and electrode thickness, the volumetric capacity of the crushed Si@TiO_2 cluster electrode is about 1100 mA h cm^{-3}, two times the volumetric capacity of commercial graphite (550 mA h cm^{-3}, Fig. 5g). The first CE is not high because the Si nano powder was still accessible to the electrolyte during the first lithiation because some of the TiO_2 shell was broken in the high pressure calendaring process and the electrolyte penetrated into the shell. The irreversible capacity contributed by the TiO_2 shell was very small (Fig. S15 and S16, ESI†).

The half-cell coulombic inefficiency over 1500 cycles is plotted in Fig. 6a on a logarithm scale. In about 20 cycles, the CI drops to a level below 0.005 (CE > 99.5%). In about 100 cycles, the CI drops to a level below 0.001 (CE > 99.9%). The read-out precision of the electrochemical testing station we used is 4 decimal digits, that is, CE_n is at best reported as 0.9999 or 1.0001, therefore we see clustering of the lowest data at 1×10^{-4} after $n > \sim 300$. This in itself does not signify

$CE_{stablized}$ reaching 99.99%, since we still have plenty of points at 2×10^{-4}, 3×10^{-4}, *etc.* What it is showing, however, is the appearance of green circles (negative CI) at approximately the same frequency as the red circles after $n \sim 800$ or so, which largely cancel out the red circles (positive CI) in the running-window average, eqn (3). A strong long-term decreasing trend of CI_n is clear in Fig. 6a, signifying the self-adaptive repair of the SiMA toward near perfect hermiticity, that is, complete prevention of liquid electrolyte flooding of any Li-active Si. Since experimentally there are temperature fluctuations and instrument noise, once $CE_{stablized}$ is below 99.99% (the instrument precision) the green circles would start to show up nearly as much as the red circles.

Fig. 6b and c compare the coulombic inefficiency of the SiMA half cell and full cell in the first 100 cycles, when the major repairs are accomplished. While CI fluctuates more in full-cell configuration, the quantitative similarity between the half- and full-cell in terms of magnitude and timescale is striking. To double-check, we "integrate" both Fig. 6b and c in the form of eqn (4), to compute the coulombic inefficiency cumulant, CIC_n, shown in Fig. 6d (red and black). Agreeing with the Fig. 6b and c comparison, the CIC curve shape and the value of the half cell and full cell are almost the same. After one hundred cycles, both CICs approach 65%, which would suggest ~60% "live" Li^+ is lost. The actual capacity loss (F_n) in the full cell was also plotted in Fig. 6d as the blue circles. The magnitude and shape of F_n were similar to CIC_n, but the eventual full-cell capacity loss (F_n) was only about 45%, lower than 65%. This gentle disagreement between F_n and CIC_n, with the actual capacity being better than the CIC projection, is intriguing. We believe that there could be several reasons for this discrepancy, as we checked earlier, eqn (6) does not hold true exactly. It could mean there is shuttling in the liquid electrolyte,[27,28] especially during mechanical adjustments of the SEI and new nSEI formation, when species other than Li^+ are soluble in the liquid electrolyte and can diffuse to the cathode and accomplish redox reactions. In any case, our full cell can indeed cycle stably with only 45% capacity loss at the 100th cycle, achieving an industrially relevant stabilized areal capacity of 1.6 mA h cm^{-2}, with a stabilized thickness of 17.8 μm that is only about 1/4 the thickness of the commercial graphite anode (55 μm). Even though the initial lithium loss is admittedly high (especially in the first 20 cycles), the full cell eventually does reach an industrially satisfactory or even excellent level of CE. During the transient stage, excess Li ions were needed to build up the self-defense, which can be accomplished cost-effectively by pre-lithiation, that is, using an additional source of "live Li" so as to not tie down the expensive and heavy transition metal elements like Co, Ni, Mn, Fe.[36]

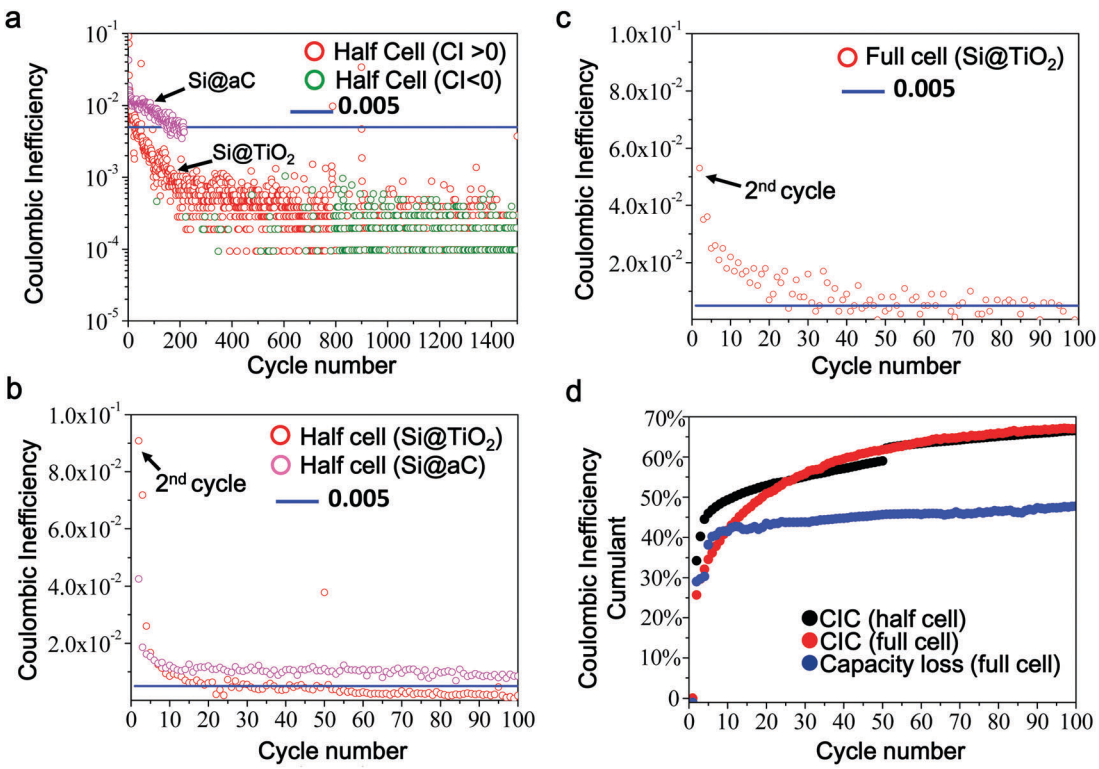

Fig. 6 Coulombic inefficiency analysis of the $Si@TiO_2$ cluster electrode. Coulombic inefficiency (CI = 1 − CE) was defined to reflect the lithium-ion loss in each cycle. (a) |CI| of the $Si@TiO_2$ cluster (half cell) over 1500 cycles (vertical axis is in logarithmic scale). Red circles stand for CI > 0, green circles stand for CI < 0. Magenta circles stand for |CI| of Si@aC (half cell) over 200 cycles. Blue line stands for CI = 0.005. (b) CI of the half cell over 100 cycles (linear coordinates). (c) CI of the $Si@TiO_2$ cluster electrode (full cell) over 100 cycles (linear coordinates). (d) Total lithium-ion loss and capacity loss percentage of the $Si@TiO_2$ cluster electrode (half cell and full cell) over 100 cycles. Lithium loss was calculated using eqn (4) based on the CI of each cycle. Capacity loss was the real measured capacity loss, eqn (5), in the lithium-constrained full cell.

In situ TEM lithiation/delithiation

The macro-tests worked well, to a degree we did not really anticipate at the beginning. To double check how the system works, we also applied *in situ* electrochemical TEM to directly monitor the structural evolution during the lithiation/delithiation of the yolk–shell Si@TiO_2 cluster. The experimental setup is schematically shown in Fig. S20a (ESI†), which is similar to that in our previous work.[42–44] Fig. S20c (ESI†) shows a series of images taken from the *in situ* lithiation/delithiation of the Si@TiO_2 cluster (Movie S5, ESI†). Initially (0 s), pristine Si nanoparticles are visible within the TiO_2 shell (15 nm). When a bias potential of +5 V was applied, the Si particles expanded in volume immediately as Li^+ diffused through the TiO_2 shell and reacted with the Si particles. As shown in the second image (53 s), the diameter of the silicon particle increased, and at this time the silicon core was just partially lithiated, forming an amorphous Li_xSi shell/crystalline Si core structure. Later, the expanding silicon touches the inner surface of the TiO_2 shell, shown in the image (84 s). With continuous lithiation, the expansive force exerted on the TiO_2 shell grew larger and larger, and the TiO_2 shell deforms to follow the expansion without gross structural failure. In the ensuing delithiation, the bias voltage changes to −5 V, silicon shrinks to almost the original size, as shown in image (253 s). Then we repeat the lithiation process (260–312 s), and find surprisingly that even at such a high rate (discharging in ∼minute, *i.e.* 60C), the TiO_2 framework still retains overall integrity despite the load transfer at the contact with Si.

The *in situ* TEM experiments revealed important details. First, although TiO_2 is thin and the void is not big enough, the TiO_2 shell can bend and later deform and not totally disintegrate. Second, the TiO_2 cluster is robust enough at the ''multicellular tissue'' level, and can stay connected during lithiation/delithiation and not disrupt the electron conduction path, which is an important electrode decrepitation mechanism. Lithium can transfer through the anatase shell and get inserted/extracted into/out of the silicon. The successful lithiation/delithiation indicates satisfactory contact between the TiO_2 shells and Si particles. Indeed, the rate of Li diffusion through the TiO_2 shell is fast enough to support 45–60C, which indicates that even though the Si core and TiO_2 shell only come into contact in a small area, high current densities and charging rates are intrinsically achievable.

Conclusions

For the first time the speed and efficacy of self-repair of a pressed yolk–shell electrode is systematically evaluated. It is shown that an exceptional degree of protection against liquid electrolyte flooding of Li-active Si can be eventually established, even though the number of cycles and the initial Li loss it takes to achieve this final condition are admittedly high. However, these are not show stoppers for SiMAs, if effective means of prelithiation can be devised, since the final electrode thickness and volumetric/gravimetric specific capacities are still much better than those of graphite. In long-term cycling, when self-healing was already completed and the aSEI + nSEI was fully sealed, the inner Si active materials will not touch the liquid electrolyte and Li ions were transferred through the aSEI + nSEI solid electrolyte, which means almost no side reaction occurs. Then the limited Li ions from the cathode can be cycled without loss for oxidation/reduction. The stabilized CE can be as high as 99.99%. From Fig. 6a it can be seen that a lot of green circles (CI < 0) appeared after several hundred cycles. Our stabilized CE actually already reached the machine precision of the battery testing equipment, and lithium consumption in the full cell can be reduced to essentially zero. The highly compressed yolk–shell Si@TiO_2 tissue, despite the unavoidable imperfections at the beginning, is surprisingly resilient functionally and can achieve a startling level of specific capacities and stabilized coulombic efficiency at low cost, making lithium-constrained full-cell cycling of a silicon-majority anode (SiMA) an imminent reality.

Experimental

Synthesis of yolk–shell Si@TiO_2 powder

First, 7 g of glucose was fully dissolved in 70 ml of DI water and then transferred to a 80 ml Teflon autoclave, then 50 mg of commercial silicon nanoparticles (<100 nm, Sigma Aldrich) was added under sonication. After 30 min of sonication, the autoclave was put in an oven at a temperature of 170 °C for 8 h. The brownish Si@C core–shell particles were harvested by three rounds of centrifugation/washing/sonication in water and absolute ethanol and subsequently dried under vacuum for more than 4 h. Generally speaking, commercial Si nanoparticles with higher uniformity and smaller diameters cost more. Here we choose relatively cheap commercial Si nanoparticles with a wide diameter range of 20–200 nm (Fig. S1a, ESI†). After the hydrothermal process in glucose solution, peanut-like Si@C structures were formed with typical diameters of 300–600 nm (Fig. S1b, ESI†). 100 mg of the Si@C core–shell particles above was dispersed in 20 mL of absolute ethanol and sonicated for about 10 min to avoid the agglomeration of the particles. Subsequently, a certain amount of titanium isopropoxide (TIPP) was added into the brownish solution and aged for about 10 h. After aging, the solution was subjected to 3 rounds of centrifugation/ethanol wash/sonication subsequently and dried in a vacuum oven for more than 8 h. The resultant powder was annealed in a furnace at 550 °C for 2 h with a heating rate of 10 °C min^{-1} and the final multi-yolks–shell Si@TiO_2 powder was obtained.

Characterization

XRD was carried out using a Bruker D8-Advance diffractometer with Ni filtered Cu Kα radiation. The applied current and voltage were 40 mA and 40 kV, respectively. During the analysis, the sample was scanned from 10 to 70° at a speed of 4° min^{-1}. SEM images were collected using a FEI Sirion scanning electron microscope (accelerating voltage 5 kV) equipped for energy-dispersive X-ray spectroscopy, and TEM images were collected

on a JEOL JEM-2010 transmission electron microscope operated at 200 kV. TG-DTA analysis was performed using a Netzsch STA 449 with an air flow at a heating rate of 10 °C min^{-1} from room temperature to 600 °C under a simulated air atmosphere (20% O_2/80% N_2, both are ultrapurity grade gases from Airgas). X-ray photoelectron spectroscopy (XPS, Phi5000 VersaProbe, Ulvac-Phi) was carried out with Al Kα radiation.

In situ transmission electron microscopy (TEM) of lithiation/delithiation

A Nanofactory TEM holder was used in the experiment. The holder was equipped with a 3D piezo-manipulator and had electrical biasing capability. Si@TiO_2 clusters were attached to a tungsten probe using a conducting epoxy (Chemtronics CW2400) and mounted on one side of the holder. On the other side, we mounted another tungsten rod after scratching a piece of Li metal to transfer a small piece of Li to the tip. The Si@TiO_2 clusters and the piece of Li metal were brought into contact inside the TEM. By applying a voltage to the working electrode (Si@TiO_2 clusters) *versus* the counter electrode (Li), Li^+ ions diffuse through the oxide/nitride layer on the Li metal and react with the Si@TiO_2 particles at the working electrode. To drive the Li^+ into Si@TiO_2, a bias of −5.0 V was applied to the working electrode with respect to the Li metal for the lithiation, and +5.0 V was used for the delithiation. The experiment was performed using a JEOL 2010F TEM operated with a 200 kV acceleration voltage. The movies in the ESI† were recorded at a rate of 5 frames per s.

In situ TEM compression experiments

A similar setup to that described above was used for the compression test of the C and TiO_2 shells and Si@TiO_2 cluster. An atomic force microscopy (AFM) probe (Nanosensors PPP-NCHR) with a spring constant of 30 N m^{-1} was attached to the tip of the gold wire using a conducting epoxy (Chemtronics CW2400). Either the aC or TiO_2 shells or the Si@TiO_2 cluster was attached to the tungsten probe by bringing the tungsten probe with conducting epoxy on the tip into contact with the powder of the shells. The gold wire and the tungsten probe were then mounted on a Nanofactory STM-TEM holder. Using the 3D piezo-manipulator, the shell was brought into contact with the cantilever tip and compression was applied to the shell by giving a displacement (D) against the cantilever. The schematic illustration of the setup and the TEM image are shown in Fig. 3a. The force acting on the shell was calculated by measuring the deflection of the cantilever tip during the compression. Other conditions were the same as those used in the lithiation/delithiation experiment.

Electrode fabrication

The SiMA electrode was prepared by mixing Si@TiO_2 (70.0 wt%), 15.0 wt% conductive carbon black (Super C65, Timcal), and 15.0 wt% poly(vinylidene fluoride) binder (Sigma-Aldrich) in *N*-methyl-2-pyrrolidinone solvent (Sigma-Aldrich). The obtained slurry was coated onto 15 μm thickness copper foil and dried at 60 °C in a vacuum oven for 12 h. The samples were then pressed (20 MPa for half cell and 30 MPa for full cell) and cut into 1 cm^2 disks at a mass loading of 0.8–2.1 mg cm^{-2} (active material, including Si and TiO_2). For pressing, the cast electrode was placed between two pieces of Cu foil and transferred into a cold pressing machine (MTI). The applied pressure is displayed on the pressure gauge. Before pressing, the thickness of Si@TiO_2 cast onto the Cu foil was 50 μm, which changed to 14.7 μm after pressing. 2032 coin cells were assembled in an Ar-filled glovebox using these working electrodes with a polymer separator (Celgard 2250). Li metal (Alfa Aesar) was used as the counter electrode (half cell) and lithium cobalt oxide (LCO) was used as the cathode (full cell). 80 μL of 1.0 M $LiPF_6$ in 89 vol% 1 : 1 w/w ethylene carbonate/diethyl carbonate (BASF Selectilyte LP40) with 10 vol% fluoroethylene carbonate and 1 vol% vinylene carbonate (Novolyte Technologies) was added as the electrolyte. The full cell configuration consists of Si@TiO_2 clusters as the anode and LCO as the cathode. The mass loading of the Si@TiO_2 electrode (11 mm diameter) was 2.1 mg cm^{-2}, giving an stable areal capacity of 2.0 mA h cm^{-2} at a current density of 0.7 mA cm^{-2} (initial discharge capacity: 3.0 mA h cm^{-2}) (Fig. S10, ESI†) when Li metal was used as the counter electrode. The stable areal capacity of the LCO cathode (9 mm diameter) tested with Li metal as the counter electrode was 2.6 mA h cm^{-2} (initial charge capacity of 3.0 mA h^{-1}) at a current density of 0.7 mA cm^{-2} (Fig. S11, ESI†). The initial CE of LCO was 94.5%. Charge/discharge rates were calculated based on silicon's theoretical capacity (4200 mA h g^{-1} Si). All the coin cells were loaded into a battery test (LAND 2001 CT battery tester) and cycled between 0.01 and 1 V (half cells) and 2.8 and 4.2 V (full cells).

Author contributions

J. L. and Y. C. conceived the project. Y. J. and S. L. synthesized samples and performed the battery tests. A. K. conducted all the *in situ* TEM measurements. J. S. and R. F. Z. performed the characterization. All authors analyzed the data and contributed to the discussion. Y. J., S. L., Y. C. and J. L. wrote the manuscript.

Acknowledgements

J. L. acknowledges support from NSF DMR-1410636 and DMR-1120901. Y. C. acknowledges the support from the Assistant Secretary for Energy Efficiency and Renewable Energy, Office of Vehicle Technologies of the U. S. Department of Energy under the Battery Materials Research (BMR) Program. Y. J. acknowledges the support from the Chinese Scholarship Council.

Notes and references

1 M. Armand and T. J. M. Arascon, *Nature*, 2008, **451**, 652.
2 A. S. Arico, P. Bruce, B. Scrosati, J. M. Tarascon and V. W. Schalkwijk, *Nat. Mater.*, 2005, **4**, 366.
3 C. K. Chan, H. Peng, G. Liu, K. McIlwrath, X. F. Zhang, R. A. Huggins and Y. Cui, *Nat. Nanotechnol.*, 2008, **3**, 31.

4 I. H. Son, J. H. Park, S. Kwon, S. Park, M. H. Rümmeli, Al. Bachmatiuk, H. J. Song, J. Ku, J. W. Choi, J. Choi, S. G. Doo and H. Chang, *Nat. Commun.*, 2015, **6**, 7393.

5 C. M. Wang, X. L. Li, Z. G. Wang, W. Xu, J. Liu, F. Gao, L. Kovarik, J. G. Zhang, J. H. Howe, D. J. Burton, Z. Y. Liu, X. C. Xiao, S. Thevuthasan and D. R. Baer, *Nano Lett.*, 2012, **12**, 1624.

6 M. N. Obrovac, L. Christensen, D. B. Le and J. R. Dahn, *J. Electrochem. Soc.*, 2007, **154**, A849.

7 F. F. Shi, Z. C. Song, P. N. Ross, G. A. Somorjai, R. O. Ritchie and K. Komvopoulos, *Nat. Commun.*, 2016, **7**, 11886.

8 M. Y. Nie, D. P. Abraham, Y. J. Chen, A. Bose and B. L. Lucht, *J. Phys. Chem. C*, 2013, **117**, 13403.

9 C. K. Chan, R. Ruffo, S. S. Hong, R. Huggins and Y. Cui, *J. Power Sources*, 2009, **189**, 1132.

10 S. Chen, P. Bao, X. Huang, B. Sun and G. Wang, *Nano Res.*, 2014, **7**, 85.

11 X. L. Li, M. Gu, S. Y. Hu, R. Kennard, P. F. Yan, X. L. Chen, C. M. Wang, M. J. Sailor, J. G. Zhang and J. Liu Li, *Nat. Commun.*, 2014, **5**, 5105.

12 M. Gu, Y. Li, X. L. Li, S. Y. Hu, X. W. Zhang, W. Xu, S. Thevuthasan, D. R. Baer, J. G. Zhang, J. Liu and C. M. Wang, *ACS Nano*, 2012, **6**, 8439.

13 Y. Li, K. Yan, H. W. Lee, Z. D. Lu, N. Liu and Y. Cui, *Nat. Energy*, 2016, **1**, 15029.

14 Y. M. Sun, N. Liu and Y. Cui, *Nat. Energy*, 2016, **1**, 16071.

15 H. Wu, G. Zheng, N. Liu, T. J. Carney, Y. Yang and Y. Cui, *Nano Lett.*, 2012, **12**, 904.

16 B. Wang, X. Li, X. Zhang, B. Luo, Y. Zhang and L. Zhi, *Adv. Mater.*, 2013, **25**, 3560.

17 X. Zhou, Y. X. Yin, L. J. Wan and Y. G. Guo, *Chem. Commun.*, 2012, **48**, 2198.

18 S. Chen, M. L. Gordin, R. Yi, G. Howlett, H. Sohna and D. H. Wang, *Phys. Chem. Chem. Phys.*, 2012, **14**, 12741.

19 J. Y. Luo, X. Zhao, J. S. Wu, H. D. Jang, H. H. Kung and J. X. Huang, *J. Phys. Chem. Lett.*, 2012, **3**, 1824.

20 L. Y. Beaulieu, K. W. Eberman, R. L. Turner, L. J. Krause and J. R. Dahn, *Electrochem. Solid-State Lett.*, **4**, A137.

21 H. Wu, G. Chan, J. W. Choi, I. Ryu, Y. Yao, M. T. McDowell, S. W. Lee, A. Jackson, Y. Yang, L. B. Hu and Y. Cui, *Nat. Nanotechnol.*, 2012, **7**, 310–315.

22 N. Liu, H. Wu, M. T. McDowell, Y. Yao, C. M. Wang and Y. Cui, *Nano Lett.*, 2012, **12**, 3315.

23 D. C. Lin, Z. D. Lu, P. C. Hsu, H. R. Lee, N. Liu, J. Zhao, H. T. Wang, C. Liu and Y. Cui, *Energy Environ. Sci.*, 2015, **8**, 2371.

24 N. Liu, Z. D. Lu, J. Zhao, M. T. McDowell, H. W. Lee, W. T. Zhao and Y. Cui, *Nat. Nanotechnol.*, 2014, **9**, 187.

25 M. J. Mayo, R. W. Siegel, A. Narayanasamy and W. D. Nix, *J. Mater. Res.*, 1990, **5**, 1073.

26 H. Ren, R. B. Yu, J. Y. Wang, Q. Jin, M. Yang, D. Mao, D. Kisailus, H. J. Zhao and D. Wang, *Nano Lett.*, 2014, **14**, 6679.

27 S. Li, J. J. Niu, Y. C. Zhao, K. P. So, C. Wang, C. A. Wang and J. Li, *Nat. Commun.*, 2015, **6**, 7872.

28 Z. Zhu, A. Kushima, Z. Y. Yin, L. Qi, K. Amine, J. Lu and J. Li, *Nat. Energy*, 2016, **1**, 16111.

29 S. Li, S. O. Halperinb and C. A. Wang, *Mater. Chem. Phys.*, 2015, **149**, 1.

30 X. M. Sun and Y. D. Li, *Angew. Chem., Int. Ed.*, 2004, **43**, 597.

31 Q. Wang, *et al.*, Monodispersed hard carbon spherules with uniform nanopores, *Carbon*, 2001, **39**, 2211–2214.

32 X. M. Sun and Y. D. Li, *J. Colloid Interface Sci.*, 2005, **291**, 7.

33 V. Privman, *Ann. N. Y. Acad. Sci.*, 2009, **1161**, 508.

34 V. K. Lamer, *Ind. Eng. Chem.*, 1952, **44**, 1270.

35 V. K. Lamer and R. H. Dinegar, *J. Am. Chem. Soc.*, 1950, **72**, 4847.

36 J. Zhao, Z. D. Lu, H. T. Wang, W. Liu, H. W. Lee, K. Yan, D. Zhuo, D. C. Lin, N. Liu and Y. Cui, *J. Am. Chem. Soc.*, 2015, **137**, 8372.

37 J. Zhao, H.-W. Lee, J. Sun, K. Yan, Y. Liu, W. Liu, Z. Lu, D. Lin, G. Zhou and Y. Cui, *Proc. Natl. Acad. Sci. U. S. A.*, 2016, **113**, 7408–7413.

38 Y. Sun, H.-W. Lee, Z. W. Seh, N. Liu, J. Sun, Y. Li and Y. Cui, *Nat. Energy*, 2016, **1**, 15008.

39 S. Dalavia, P. Gudurub and B. L. Luchta, *J. Electrochem. Soc.*, 2012, **159**, A642–A646.

40 C. Xu, F. Lindgren, B. Philippe, M. Gorgoi, F. Björefors, K. Edström and T. Gustafsson, *Chem. Mater.*, 2015, **27**, 2591–2599.

41 L. Chen, K. Wang, X. Xie and J. Xie, *Electrochem. Solid-State Lett.*, 2006, **9**, A512–A515.

42 A. Kushima, X. H. Liu, G. Zhu, Z. L. Wang, J. Y. Huang and J. Li, *Nano Lett.*, 2011, **11**, 4535.

43 J. Y. Huang, L. Zhong, C. M. Wang, J. P. Sullivan, W. Xu, L. Q. Zhang, S. X. Mao, N. S. Hudak, X. H. Liu, A. Subramanian, H. Y. Fan, L. Qi, A. Kushima and J. L. Huang, *Science*, 2010, **330**, 1515.

44 X. H. Liu, Y. Liu, A. Kushima, S. L. Zhang, T. Zhu, J. Li and J. Y. Huang, *Adv. Energy Mater.*, 2012, **2**, 722.